Biophysical Journal, Volume *114*

Supplemental Information

Protein Flexibility and Synergy of HMG Domains Underlie U-Turn Bending of DNA by TFAM in Solution

Anna Rubio-Cosials, Federica Battistini, Alexander Gansen, Anna Cuppari, Pau Bernadó, Modesto Orozco, Jörg Langowski, Katalin Tóth, and Maria Solà

Supporting Figures

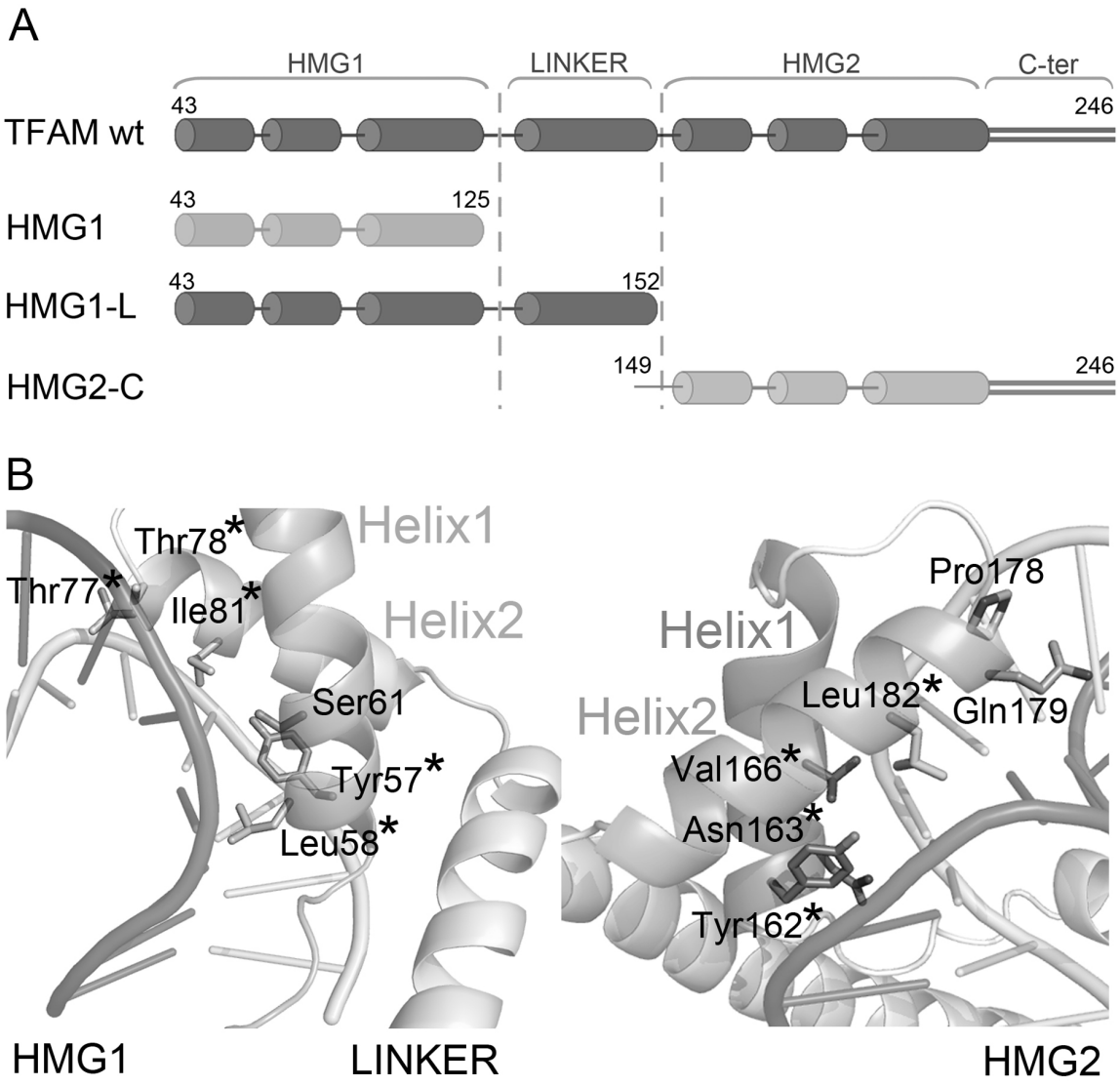

Figure S1. TFAM constructs and relevant regions. (A) Schematic representation of full length TFAM and TFAM domains HMG1 (residues 44-125), HMG1-L (43-152) and HMG2-Cter (149-246) used in smFRET experiments. **(B)** Local interactions of TFAM with DNA. Residues that are in direct contact with DNA bases are shown as sticks in HMG1 (Ser61, Tyr57, Leu58, Thre77, Thr78 and Ile81) and HMG2 (Tyr162, Asn163, Val166, Pro178, Gln179 and Leu182). Residues labelled with black asterisks were mutated to alanine for MD simulations.

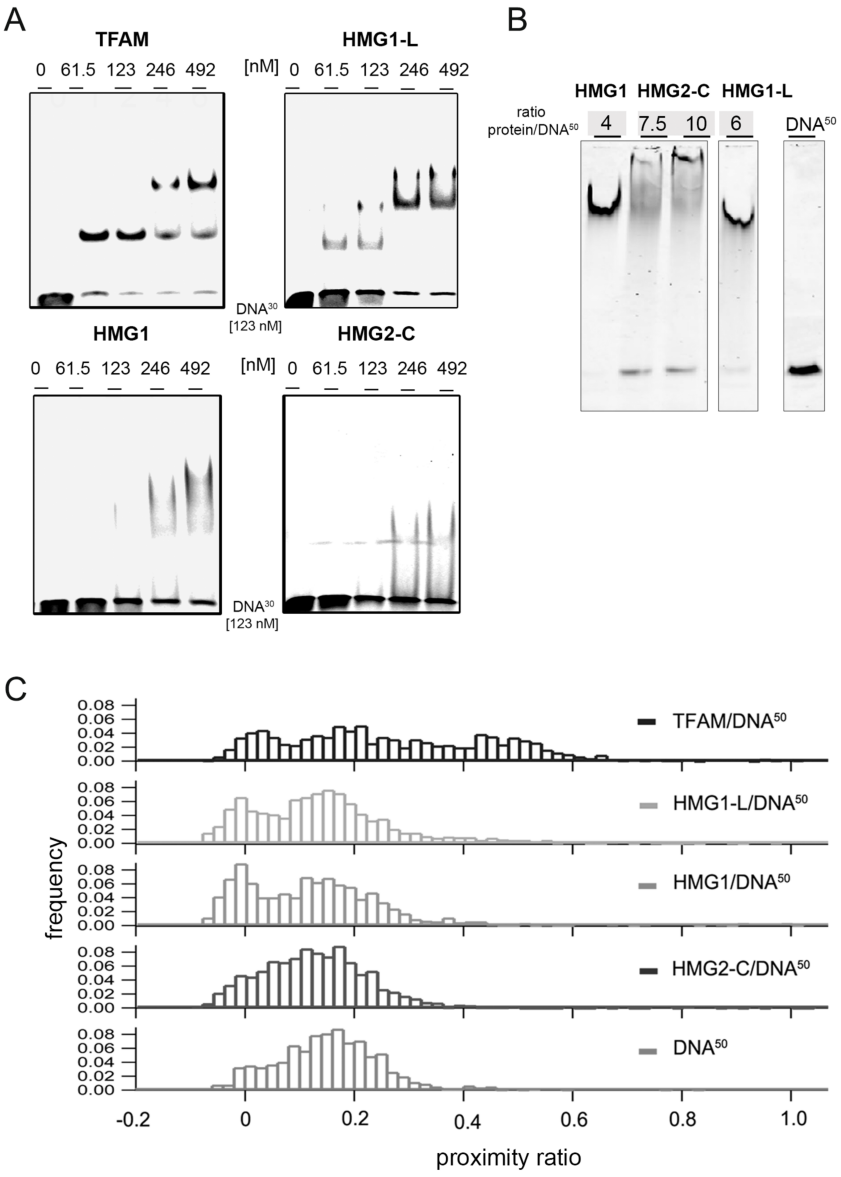

Figure S2. TFAM and TFAM domains do not bind equally strong to DNA. (A) EMSA assays for full-length TFAM and TFAM domains (HMG1-L, HMG1 and HMG2-Cter) with Alexa 594-labelled DNA^{30}. From left to right, protein concentration is increased from 0 to 492 nM versus constant DNA amounts of 123 nM. The gel bands were visualized using the fluorescence signal from Alexa 594 (excitation at 532 nm, detection at 595-625 nm). TFAM shows a higher binding ability than the isolated domains (HMG1 and HMG2-Cter) as it generates well-defined bands with no smear. (**B**) EMSA of TFAM domains HMG1, HMG2-Cter and HMG1-L to DNA^{50} labelled with Alexa 488 and Alexa 594. Complexes were run on a 5% polyacrylamide native gel. The gel bands were visualized by Alexa 594 emission. All TFAM domains bind to labelled-DNA^{50}, and HMG2-C shows the weakest binding. (**C**) Exemplary smFRET histograms for TFAM and TFAM domains in complex with DNA^{50}. Full-length TFAM is shown on top, and HMG1-L, HMG1 and HMG2-Cter in complex with DNA^{50} are shown below. The proximity ratio distribution for free DNA is shown for comparison at the bottom of the panel.

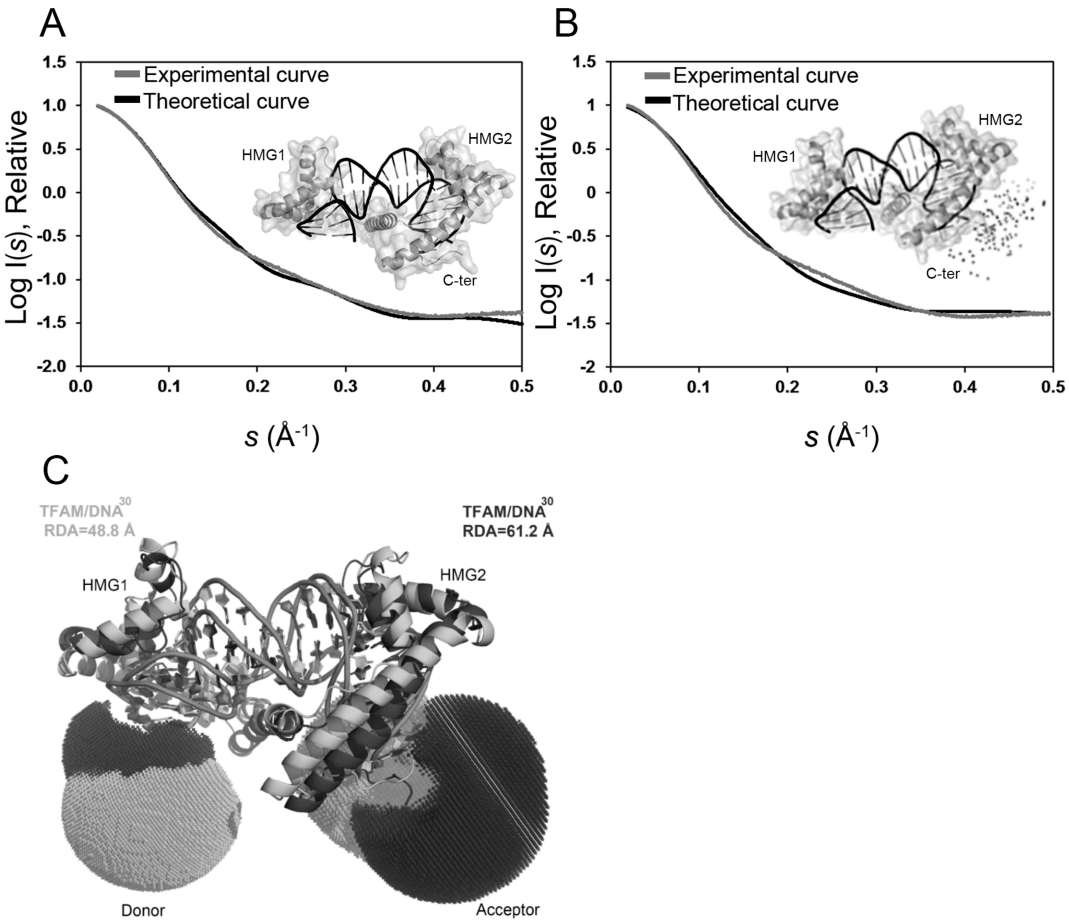

Figure S3. Structural flexibility of the TFAM/LSP complex. **(A)** SAXS analysis of the TFAM/LSP complex. Comparison of the experimental scattering profile (in black) and a theoretical curve based on the TFAM/LSP crystal structure (in grey). The crystallographic structure used to calculate the theoretical curve is shown. Both curves are represented in logarithmic scale as a function of the momentum transfer, $s = 4\pi\sin(\theta)/\lambda$ (2θ, scattering angle; X-ray wavelength $\lambda = 1.5$ Å). The theoretical curve was calculated using CRYSOL. Despite the similarity of both curves, the overall agreement is poor ($\chi 2 = 2.93$), which suggests the presence of intrinsic structural flexibility. **(B)** The same as in (A) but using a subensemble of 50 conformations with full flexibility at TFAM's C-terminal tail (residues Gly226-Cys246). The 50 conformations subensemble used to calculate the theoretical curve are also shown, flexible C-ter$^{\alpha}$ represented as dots. **(C)** Flexibility of TFAM-LSP complex leads to variations in interdye distance. Modelling of interdye distance for two representative TFAM/DNA^{30} structures: the LSP-22 crystal structure (in light grey) and the conformation from the MD simulation that showed the highest *rmsd* divergence from the crystal structure (in dark grey). The accessible volumes of the fluorophores were modelled using the FPS toolkit (1).

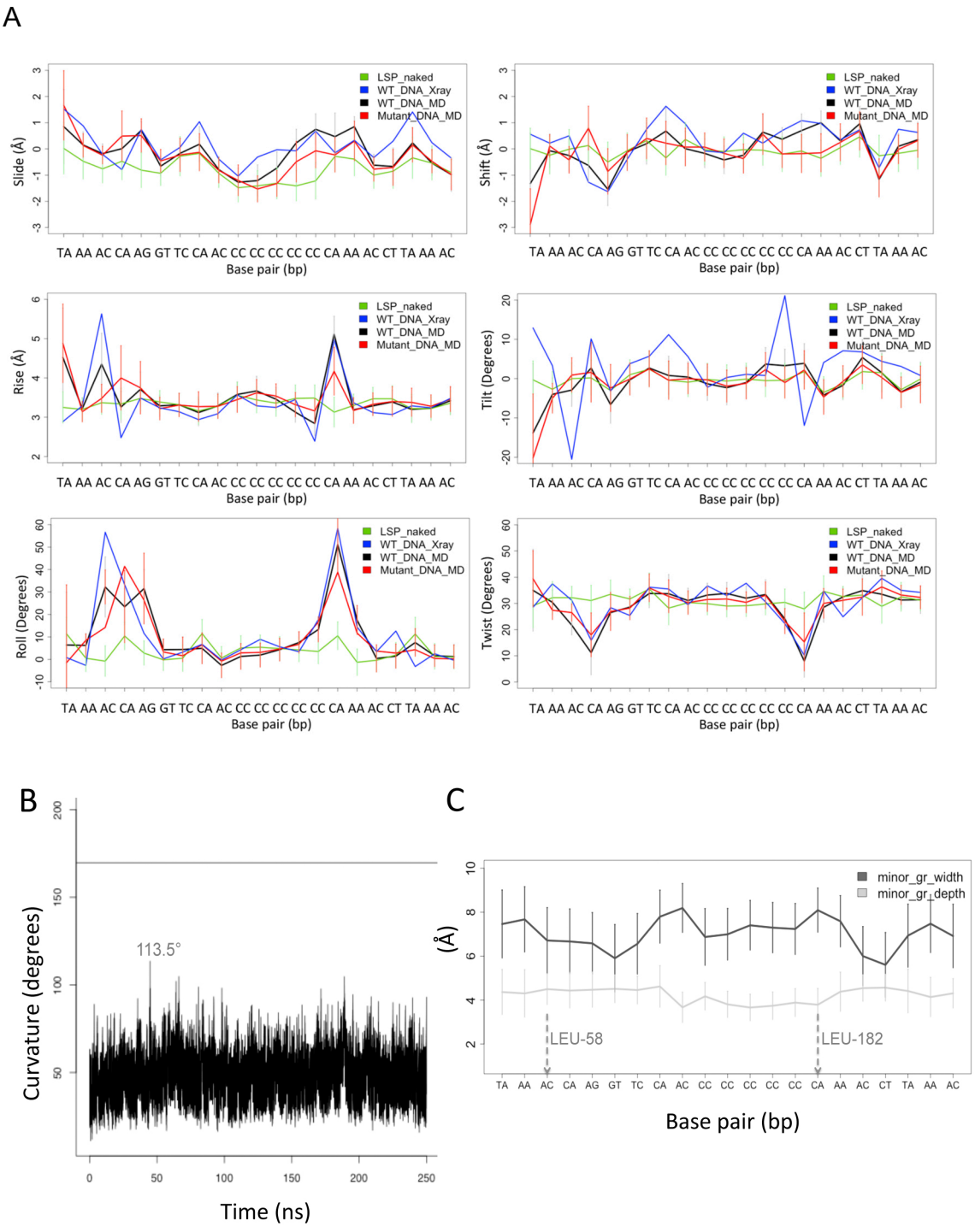

Figure S4. Properties of protein-bound and naked DNA. **(A)** Base pair translational (shift, slide and rise) and rotational (tilt, roll and twist) parameters for the LSP sequence in the X-ray crystal structure (blue) and averaged during the MD simulations for unbound DNA (green), DNA in complex with the wild type

(WT) protein (black) and DNA in complex with the MD-mutant (red). **(B)** Total curvature of the unbound LSP DNA[30] sequence during the MD simulation. The horizontal line at 169 degrees corresponds to the curvature of LSP in the X-ray structure of the complex. The average curvature of unbound DNA during the simulation is (47±12)°. Note that the curvature shows high peaks during the simulation, with the largest curvature reaching 113.5°. **(C)** Minor groove width and depth averaged during the MD simulation of unbound LSP DNA[30] (standard deviation represented as vertical bars). The left vertical arrow highlights the Leu58 intercalation site in the TFAM/LSP complex. This site is characterized by a narrower and slightly deeper minor groove than the Leu182 insertion site (right vertical arrow).

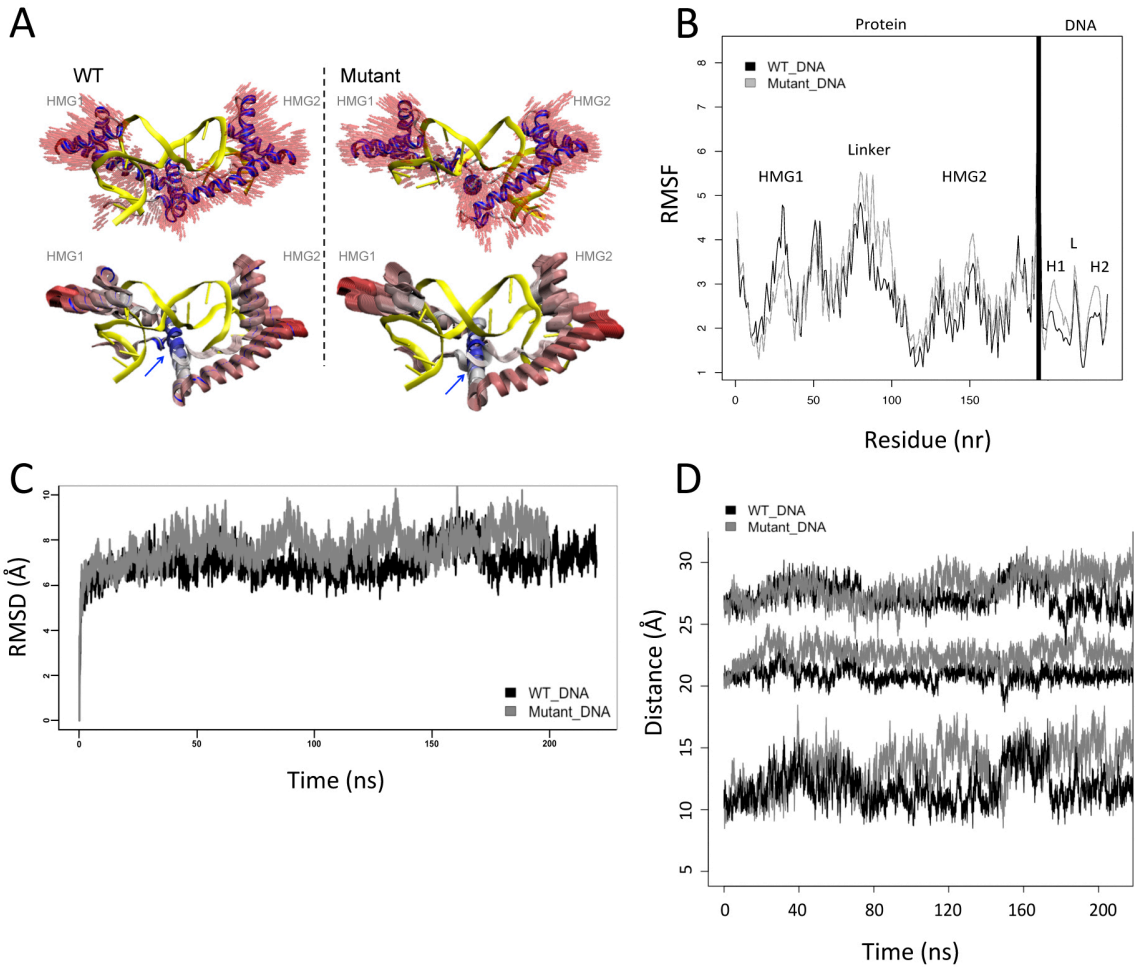

Figure S5. Comparison of the wild type and MD-mutant complexes during the MD simulation. **(A)** Representation of the movement along the PCA (principal component analysis) first normal mode for the WT (left panel) and MD-mutant (right panel) proteins within the protein/DNA complex. This first component describes a significant part of the motion during the simulation of the WT and MD-mutant (10% and 18%, respectively). The two top left and right panels show the directions of the first normal mode. In this case, the first eigenvector describes the two HMG boxes moving back and forth, in a "breathing movement". The bottom panels show the overlay of the protein structures during the MD (thicker structural segments indicate wider displacements). The highest mobility of the protein is represented in red, the lowest in blue. The helices and the HMG box L–shape elbows show highest movement; the hinge point is located in the middle of the linker region (indicated with blue arrows in both panels) around which the protein domains move. The relative movements of the DNA have not been represented for clarity. **(B)** Root mean square fluctuations (RMSF) values of each residue in WT (black line) and MD-mutant (grey line) complexes. The RMSF were computed along the MD simulations for both complexes. The HMG1, HMG2 and linker regions are indicated. H1, H2 and L indicate the DNA regions that contact the corresponding protein domains HMG1, HMG2 and linker, respectively. **(C)** Time-dependent root mean square deviation (RMSD) of all protein-DNA heavy atoms from the WT and the MD-mutant complexes (in black and grey, respectively). The RMSD values were computed relative to the initial crystal structure after relaxation. **(D)** Distance between the protein and the DNA, for the WT (in black) and MD-mutant (in grey) complexes. From top to bottom, distances related to HMG1, HMG2 and the linker are

shown, respectively. Note that for the MD-mutant, HMG2 slightly separates from the DNA at the beginning and during the whole simulation. HMG1 shows similar distances in both complexes. In contrast, the linker shows a prominent irreversible separation in the MD-mutant.

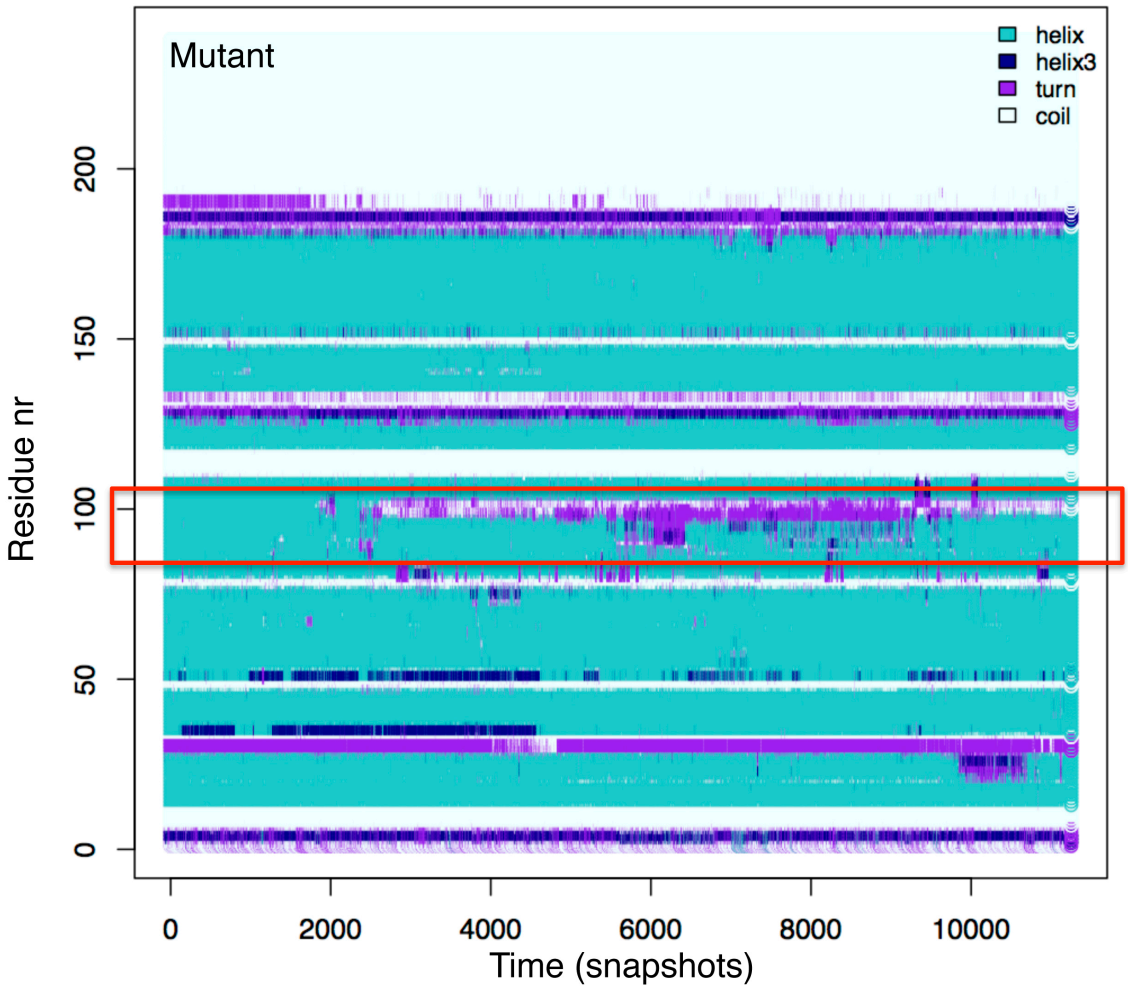

Figure S6. Variability of the MD-mutant secondary structure during the simulation (every 100th snapshot). The secondary structure is maintained except for the linker (red frame) that irreversibly unfolds from the helix conformation (in cyan) to turn or coil (in violet or white, respectively).

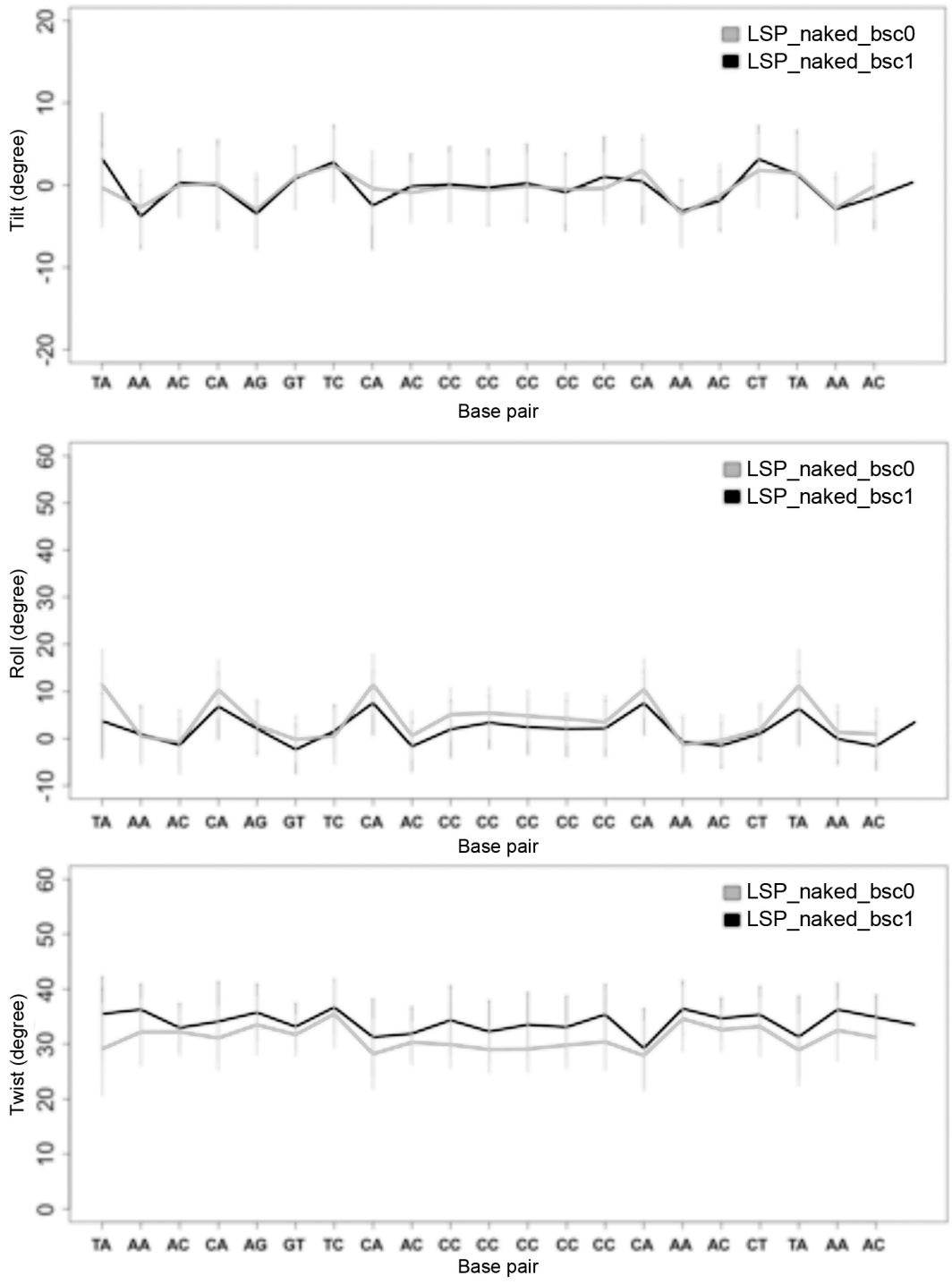

Figure S7. Comparison of the time-averaged base pair rotational parameters (tilt, roll and twist in degrees) for unbound DNA[30] (LSP_naked) during the MD simulations using the force fields parmBSC0 (in grey) and parmBSC1 (in black), respectively.

Supporting Materials and Methods

Design of DNA constructs for smFRET experiments

To determine whether TFAM bends DNA in a U- or a V-shape, we performed smFRET experiments on TFAM in complex with 30 bp (DNA^{30}) and 50 bp (DNA^{50}) long DNAs. Both constructs were centred on the TFAM cognate binding sequence LSP22 and flanked by the corresponding mtDNA sequences on either side, (see Figure 1). The donor fluorophore (Alexa 488) was attached to the 5' end of the cytosine-rich DNA strand, the acceptor (Alexa 594) to the 5' end of the complementary strand. The use of a hexamethylene linker ensured rotational freedom of the dyes. Since the crystal structure predicts that, at the inner U-turn face, the DNA ends are within 20 Å of each other, we intended to place the dyes at the outer face of the U- or V-turn, to minimize the risk of self-quenching at very short distances. The dyes were chosen because a) their Förster radius (R_0 = 55.6 Å) is of the order of the expected interdye distance after protein binding, enabling high sensitivity, and b) their emission peaks are separated by 100 nm (519 nm for Alexa 488 *vs.* 617 nm for Alexa 594), allowing spectral separation with little cross talk. Labelled single DNA strands were purchased from *IBA*, purified by reverse phase HPLC and annealed in TE buffer (10 mM Tris-HCl, 0.1 mM EDTA, pH = 7.5) with 100 mM NaCl. Samples were heated to 90°C for 5 minutes and cooled to room temperature overnight; the duplex was then separated from non-annealed DNA by HPLC. The sequences of the oligonucleotides were: DNA^{30}: 5'-(Alexa 488)*TC TTT TAA CAG TCA CCC CCC AAC TAA CAC A-3' and 5'-(Alexa 594)*T GTG TTA GTT GGG GGG TGA CTG TTA AAA GA; DNA^{50}: 5'-(Alexa 488)*TGC GGT AG CAC TTT TAA CAG TCA CCC CCC AAC TAA CAC ATT ATT TTC CA-3' and 5'-(Alexa 594)*TC GAA AAT AA GTG TTA GTT GGG GGG TGA CTG TTA AAA GTG CAT ACC GCA. Additional control samples were prepared with the same DNA sequences carrying only the donor fluorophore (donor-only) or only the acceptor fluorophore (acceptor-only).

Protein preparation

TFAM (residues 43-246; UniProt Q00059) was produced as previously reported (2). TFAM domains (Supplementary Figure 1A) HMG1 and HMG2-Cter (residues 44-125 and 149-246, respectively) were cloned into the expression vector pET28b(+) (*Novagen*). The HMG1-L domain (residues 43-152) was cloned using the *In-Fusion*^{TM} system in a pOPINF vector that added an N-terminal 6-histidine tag. TFAM domains were prepared as the WT protein (2), and their folding assessed by circular dichroism at the Biomolecular Screening and Protein Technologies Unit at the Center for Genomic Regulation (CRG, Barcelona, Spain).

Protein and DNA complex formation

The high salt concentration in the protein purification buffer (50 mM HEPES pH 7.5, with 750 mM NaCl, and 5 mM DTT) (2) impairs TFAM/DNA interaction. Therefore, DNA and protein (or protein domains) were mixed at different molar ratios (1:1, 2:1) and dialyzed in three dialysis steps (the last one overnight) against buffers with lower salt down to 100 mM NaCl. After dialysis, the complex formation was checked on a native polyacrylamide gel (see below). For DNA binding assays, complexes at different protein:DNA ratios were incubated on ice for 20 minutes (10 µl final volume).

smFRET measurements require less than 100 pM of labelled sample to ensure single molecule discrimination. To minimize complex dissociation at such low concentrations we added a ten-fold excess of unlabelled complexes to the labelled ones. smFRET experiments were performed at 500 pM total DNA (50 pM of which were labelled). The smFRET buffer consisted of 50 mM Tris pH 7.5, with 100 mM NaCl, 0.01% NP40 to prevent sample aggregation and adsorption to the chamber walls and 1 mM ascorbic acid to improve the photostability of the dyes. The buffer was freshly prepared before each set of experiments and filtered through a polycarbonate membrane with a cut-off of 0.02 µm. Additionally, buffer conditions were optimized by lowering the DTT concentration from 5 mM to 1 mM for smFRET experiments, because biological reducing agents like DTT decrease dye stability (3).

Electrophoretic mobility shift assays

EMSAs were used to check complex formation after dialysis and for DNA binding assays with protein domains. After incubation of protein and DNA for complex formation (see above), samples were loaded on a non-denaturing polyacrylamide gel (5% polyacrylamide, 0.5 x Tris-Borate-EDTA [TBE] buffer). An electric field of 10 V cm^{-1} was applied for 1 h at 4 °C. DNA bands were visualized using either fluorescently labelled or non-labelled DNA. Gels were imaged on a Typhoon 9400 scanner with appropriate filter settings. Double-labelled samples were imaged in three spectral windows (donor channel: excitation at 488 nm, detection at 500–540 nm; acceptor channel: excitation at 532 nm, detection at 595–625 nm; transfer channel: excitation at 488 nm, detection at 595–625 nm). Acceptor-only labelled DNA was visualized using the acceptor channel only. For unlabelled DNA samples, gels were stained with SyBr Gold (Invitrogen) to visualize protein/DNA complexes.

Single molecule FRET experiments

smFRET experiments were performed on a home-built confocal microscope as described in (4, 5). The donor dye (Alexa 488) was excited at 491 nm with a continuous-wave DPSS-laser (Cobalt), whose beam was focused to a diffraction-limited spot by a 60x / NA = 1.2 objective (UPlanApo, Olympus). Donor and acceptor emission were detected in epifluorescence, separated from scattered laser light by a dichroic beam splitter (505DRLP) and imaged onto a 100 µm pinhole, which rejected any out-of-focus light. The effective

observation volume of this setup was about 1 fl. Transmitted fluorescence was split into two detection channels (donor signal: 500-540 nm, acceptor signal 610-700 nm) defined by an infrared blocking filter (700CFSP), a dichroic beam splitter (580DRLP) and appropriate interference filters (donor channel: 520DF40, transfer channel: 610ALP, all filters and dichroic beam splitters from Omega Optical). The signals from the two avalanche photodiodes (SPAD-AQ-14, Perkin-Elmer) were read by a time-correlated single photon counting (TCSPC) board (TimeHarp200, Picoquant) and processed by our own software. The single photon data stream was smoothed by a Lee filter and single molecules were identified as bursts of at least 50 photons with a mutual separation of less than 120 µs. For each burst several parameters were recorded, including the proximity ratio P, see equation S2, burst duration and photon intensity per time. Single molecule distributions of the proximity ratio and other parameters were built and further analysed with IGOR Pro software (WaveMetrics).

Calculation of the proximity ratio from the smFRET measurements

Energy transfer was analysed via the sensitized emission of the acceptor upon selective donor excitation (6). In smFRET, the proximity ratio P, as a measure of energy transfer, is estimated from the detected photon numbers in the donor and acceptor channel per burst, N^0_D and N^0_T. These raw intensities contain contributions from background (B_D and B_T) and donor crosstalk into the acceptor channel (α_{DT}) which have to be corrected for, giving corrected intensities N_D and N_T:

$$\begin{aligned} N_T &= \left(N_T^0 - B_T\right) - \alpha_{DT}\left(N_D^0 - B_D\right) \\ N_D &= \left(N_D^0 - B_D\right) \end{aligned} \qquad \text{(S1)}$$

The proximity ratio is then calculated as

$$P = \frac{N_T}{N_T + N_D} \qquad \text{(S2)}$$

All correction factors were determined in independent control experiments with a donor-only sample and pure buffer solution. For background correction, we first computed the average count rate of background photons for the buffer solution, B_D and B_T, as photons per millisecond. For the i-th single molecule event, b_D and b_T are then multiplied with the duration of the i-th burst, d_i, to yield

$$B_{D,T}{}^{i} = b_{D,T} \cdot d^{i}. \qquad \text{(S3)}$$

Donor crosstalk into the acceptor channel is corrected for by an independent measurement of a donor-only sample that is measured for 5-10 minutes to build a histogram of the proximity ratio P. After background subtraction, the peak value in the P histogram, $P_{D\text{-only}}$, yields the crosstalk factor as

$$\alpha_{DT} = \frac{1}{{}^{1}/_{P_{D-only}} - 1} \quad \text{(S4)}$$

In our analysis, we did not include an additional correction for direct acceptor excitation, since we were only interested in relative changes in P distribution between samples.

SAXS measurements

Small-angle X-ray scattering (SAXS) data of TFAM/LSP22 at 1.7, 3.9 and 10.5 mg mL^{-1} were measured at the BioSAXS beamline BM29 at the European Synchrotron Research Facility (ESRF) in Grenoble, France. Samples were prepared in 50 mM HEPES pH 7.5, 20 mM NaCl, 5 mM DTT, 10% glycerol. For each sample, data were collected in 10 frames of 1 s, at 20°C. Sample scattering curves were averaged and subtracted from the buffer scattering curves using standard procedures (7). Curves obtained at the three concentrations were merged into a single curve that was used for further analysis. The forward scattering intensity $I(0)$ and the radius of gyration R_g were calculated with the Guinier approximation assuming that, at very small angles ($s < 1.3/R_g$), intensity is represented as $I(s) = I(0)\exp(-(sR_g)2/3)$. The molecular weight of the particle was calculated with Scåtter (8). The maximum particle dimension, D_{max}, and the distance distribution were calculated from the scattering pattern with program GNOM (9) using the momentum transfer range $0.015 < s < 0.50$ $Å^{-1}$. The SAXS profile was compared with the crystallographic structure using the program CRYSOL (10). The Ensemble Optimization Method (EOM) was used to study the conformational variability of the TFAM/LSP complex (11). EOM selects from a large pool of random conformations (10,000) a subensemble (50 conformations) that collectively describes the experimental SAXS curve. A large pool of TFAM/LSP conformations was built by adding flexible C-terminal tails to the crystallographic structure. These flexible chains spanning from Gly226 to Cys246 and the his-tag were obtained with Flexible-Meccano (12) and side-chains were added with SCCOMP (13). For each of these models, a theoretical SAXS profile was computed with the program CRYSOL (10) using standard parameters.

Molecular dynamics simulations

MD simulations of free DNA[30] and DNA in complex with wild type (WT) or mutant TFAM were performed using the AMBER 12 package (14). The starting coordinates of the TFAM/LSP complex were taken from the LSP22 X-ray crystal structure (PDB entry 3TQ6). The mutant variant was created by mutating all the residues of the HMG-boxes that directly interact with the DNA bases to alanine (L58A, Y57A, T77A, T78A and I81A from HMG-box1, and Y162A, N163A, V166A, L182A from HMG-box2). The topology coordinates and parameter files of free DNA, mutant and WT complexes were built using the AMBER leap module. All trajectories were obtained using *state-of-the-art* simulation conditions (15) and

the parmbsc0 refinement (16) to the AMBER parm99 force field (17, 18). Each simulated structure was solvated by placing it at the centre of an octahedron box and filling with TIP3P (19) water molecules, at a minimum solute-wall distance of 10 Å. The system was neutralized with the AMBER leap module using Na^+ as counterions. The total system size for free DNA^{30} was 1905 DNA atoms, 58 Na^+ and 37140 water molecules; for wild type/LSP 4721 protein-DNA atoms, 26 Na^+ counter-ions, and 60383 water atoms; and for MD-mutant/LSP 4654 protein-DNA atoms, 26 Na^+ counter-ions, and 60350 water atoms. Each system was simulated in periodic boundary conditions. Electrostatic interactions were calculated with the particle mesh Ewald method (20). The SHAKE algorithm (21) was used to constrain all bond lengths involving hydrogen atoms at their equilibrium values.

Solvent and ions were initially optimized and relaxed by keeping the solute atoms constrained to their initial position with decreasing force constants of 25, 20, 15, 10 and 5 kcal/(mol Å), using our published multistep protocol (22),(23). The subsequent MD procedure consisted of 100 ps of system thermalization (at T = 298 K), minimization and equilibration without any constraint for 1 ns. This was followed by a 300 ns simulation at constant temperature (298 K) and at a constant pressure of one bar at 2 fs time steps. The atomic positions were saved every 1 ps for subsequent analysis.

Trajectory analysis

The AmberTools suite of programs was used to calculate the root-mean-square deviations (RMSD), distances and root-mean-square fluctuations (RMSF) from the trajectories. The VMD program was used for the analysis of the hydrogen bonds (HBs), secondary structure and principal component analysis (24). HBs were defined using a cut-off of 3.5 Å for the distance between H-donor and H-acceptor atoms and an angle of 120 degrees between them. Physical and geometrical descriptors from the MD simulations were used to study DNA deformability at the level of individual base pair steps. Each step is geometrically described by a set of six *helical movements*: three translations (rise [s], slide [l] and shift [f]) and three rotations (twist [w], roll [r] and tilt [t]). We computed the time-averaged helical parameters as well as the curvature of free and protein-bound DNA from the MD trajectories using the program Curves+ (25). The deformability during these movements is described by the stiffness constants (k_i) associated with the displacements with respect to each helical parameter at the equilibrium. The values for the parameters describing the equilibrium geometry and stiffness constants of naked and protein-bound DNA were derived from long atomistic MD simulations of DNA^{30} sequence in water, free (250 ns) or bound (200 ns) to wild type or to mutant TFAM. In detail, to obtain the equilibrium values and associated force constants of each helical parameter for each base pair step, DNA geometries extracted from the MD simulations were projected into a helical reference system using Curves (25). By collecting the values of these helical parameters during the MD, we built a covariance matrix, *C*h, in helical space for each unique base pair step. The inversion of the covariance matrix, multiplied by the Boltzmann constant *(k_B)* and the absolute temperature (*T), gives* stiffness matrices Ξ_h:

$$\Xi_{\mathrm{h}} = k_{\mathrm{B}} T C_{\mathrm{h}}^{-1} = \begin{bmatrix} k_{\mathrm{twist}} & k_{t-r} & k_{t-l} & k_{t-i} & k_{t-s} & k_{t-d} \\ k_{t-r} & k_{\mathrm{roll}} & k_{r-l} & k_{r-i} & k_{r-s} & k_{r-d} \\ k_{t-l} & k_{r-l} & k_{tilt} & k_{l-i} & k_{l-s} & k_{l-d} \\ k_{t-i} & k_{r-i} & k_{l-i} & k_{\mathrm{rise}} & k_{i-s} & k_{i-d} \\ k_{t-s} & k_{r-s} & k_{l-s} & k_{i-s} & k_{\mathrm{shift}} & k_{s-d} \\ k_{t-d} & k_{r-d} & k_{l-d} & k_{i-d} & k_{s-d} & k_{\mathrm{slide}} \end{bmatrix} \quad \text{(S5)}$$

These contain the elastic force constants associated with helical deformation at the base pair step level. The diagonal elements provide the stiffness constants associated with pure rotational (twist, roll and tilt) and translational (rise, shift and slide) deformations within the given step (26),(27). A rough global estimate of each step's stiffness (k_{total}) was determined by the product of the pure stiffness constants $k_w \cdot k_r \cdot k_t \cdot k_s \cdot k_l \cdot k_f$, appearing at the diagonal of the matrix.

Calculations for the naked DNA[30] were also performed using the recent force-field parmBSC1 (28). The comparison with parmBSC0 (Supplementary Figure S7) shows that average values follow the same pattern and fall inside mutual standard deviations as previously verified (28);(29).

Supporting Material References

1. Kalinin, S., T. Peulen, S. Sindbert, P. J. Rothwell, S. Berger, T. Restle, R. S. Goody, H. Gohlke, and C. A. Seidel. 2012. A toolkit and benchmark study for FRET-restrained high-precision structural modeling. Nat Methods 9:1218-1225.
2. Rubio-Cosials, A., J. F. Sydow, N. Jimenez-Menendez, P. Fernandez-Millan, J. Montoya, H. T. Jacobs, M. Coll, P. Bernado, and M. Sola. 2011. Human mitochondrial transcription factor A induces a U-turn structure in the light strand promoter. Nature structural & molecular biology 18:1281-1289.
3. Aitken, C. E., R. A. Marshall, and J. D. Puglisi. 2008. An oxygen scavenging system for improvement of dye stability in single-molecule fluorescence experiments. Biophysical journal 94:1826-1835.
4. Gansen, A., K. Toth, N. Schwarz, and J. Langowski. 2009. Structural variability of nucleosomes detected by single-pair Forster resonance energy transfer: histone acetylation, sequence variation, and salt effects. J Phys Chem B 113:2604-2613.
5. Gansen, A., K. Toth, N. Schwarz, and J. Langowski. 2015. Opposing roles of H3- and H4-acetylation in the regulation of nucleosome structure--a FRET study. Nucleic acids research 43:1433-1443.
6. Clegg, R. M. 1992. Fluorescence resonance energy transfer and nucleic acids. Methods Enzymol 211:353-388.
7. Petoukhov, M. V., D. Franke, A. V. Shkumatov, G. Tria, A. G. Kikhney, M. Gajda, C. Gorba, H. D. Mertens, P. V. Konarev, and D. I. Svergun. 2012. New developments in the ATSAS program package for small-angle scattering data analysis. J Appl Crystallogr 45:342-350.
8. Rambo, R. P., and J. A. Tainer. 2013. Accurate assessment of mass, models and resolution by small-angle scattering. Nature 496:477-481.

9. Svergun, D. I. 1992. Determination of the regularization parameter in indirect-transform methods using perceptual criteria. J. Appl. Crystallogr. 25:495-503
10. Svergun, D. I., C. Barberato, and M. H. J. Koch. 1995. CRYSOL - a program to evaluate X-ray solution scattering of biological macromolecules from atomic coordinates. . J. Appl. Crystallogr. 28:768-773.
11. Bernadó, P., E. Mylonas, M. V. Petoukhov, M. Blackledge, and D. I. Svergun. 2007. Structural characterization of flexible proteins using small-angle X-ray scattering. Journal of the American Chemical Society 129:5656-5664.
12. Bernado, P., L. Blanchard, P. Timmins, D. Marion, R. W. Ruigrok, and M. Blackledge. 2005. A structural model for unfolded proteins from residual dipolar couplings and small-angle x-ray scattering. Proceedings of the National Academy of Sciences of the United States of America 102:17002-17007.
13. Eyal, E., R. Najmanovich, B. J. McConkey, M. Edelman, and V. Sobolev. 2004. Importance of solvent accessibility and contact surfaces in modeling side-chain conformations in proteins. J Comput Chem 25:712-724.
14. Case, D. A., V. Babin, J. T. Berryman, R. M. Betz , Q. Cai , D. S. Cerutti, T. E. I. Cheatham, T. A. Darden, R. E. Duke, and H. Gohlke. 2014. AMBER. University of California, San Francisco.
15. Perez, A., F. J. Luque, and M. Orozco. 2007. Dynamics of B-DNA on the microsecond time scale. Journal of the American Chemical Society 129:14739-14745.
16. Perez, A., I. Marchan, D. Svozil, J. Sponer, T. E. Cheatham, 3rd, C. A. Laughton, and M. Orozco. 2007. Refinement of the AMBER force field for nucleic acids: improving the description of alpha/gamma conformers. Biophysical journal 92:3817-3829.
17. Cornell, W. D., P. Cieplak, C. I. Bayly, I. R. Gould, K. M. Merz, D. M. Ferguson, D. C. Spellmeyer, T. Fox, J. W. Caldwell, and P. A. Kollman. 1995. A second generation force field for the simulation of proteins, nucleic acids, and organic molecules. J. Am. Chem. Soc. 117:5179–5197.
18. Cheatham, T. E., 3rd, P. Cieplak, and P. A. Kollman. 1999. A modified version of the Cornell et al. force field with improved sugar pucker phases and helical repeat. J Biomol Struct Dyn 16:845-862.
19. Jorgensen, W. L., J. Chandrasekhar, and J. D. Madura. 1983. J. Chem. Phys. 79:926-935.
20. Darden, T., D. York, and L. Pedersen. 1993. Particle mesh Ewald: An N · log(N) method for Ewald sums in large systems. J Chem Phys 98:10089–10092.
21. Ryckaert, J.-P., G. Ciccotti, and H. J. Berendsen. 1977. Numerical integration of the cartesian equations of motion of a system with constraints: molecular dynamics of n-alkanes. J. Comput. Phys. 23:327–341.
22. Dickerson, R. E., and H. L. Ng. 2001. DNA structure from A to B. Proceedings of the National Academy of Sciences of the United States of America 98:6986-6988.
23. Shields, G. C., C. A. Laughton, and M. J. Orozco. 1997. Molecular Dynamics Simulations of the d(T·A·T) Triple Helix. J. Am. Chem. Soc. 119:7463–7469.
24. Humphrey, W., A. Dalke, and K. Schulten. 1996. VMD: visual molecular dynamics. J Mol Graph 14:33-38, 27-38.
25. Lavery, R., M. Moakher, J. H. Maddocks, D. Petkeviciute, and K. Zakrzewska. 2009. Conformational analysis of nucleic acids revisited: Curves+. Nucleic acids research 37:5917-5929.

26. Lankas, F., J. Sponer, J. Langowski, and T. E. Cheatham, 3rd. 2003. DNA basepair step deformability inferred from molecular dynamics simulations. Biophysical journal 85:2872-2883.
27. Olson, W. K., A. A. Gorin, X. J. Lu, L. M. Hock, and V. B. Zhurkin. 1998. DNA sequence-dependent deformability deduced from protein-DNA crystal complexes. Proceedings of the National Academy of Sciences of the United States of America 95:11163-11168.
28. Ivani, I., P. D. Dans, A. Noy, A. Perez, I. Faustino, A. Hospital, J. Walther, P. Andrio, R. Goni, A. Balaceanu, G. Portella, F. Battistini, J. L. Gelpi, C. Gonzalez, M. Vendruscolo, C. A. Laughton, S. A. Harris, D. A. Case, and M. Orozco. 2016. Parmbsc1: a refined force field for DNA simulations. Nat Methods 13:55-58.
29. Dans, P. D., L. Danilane, I. Ivani, T. Drsata, F. Lankas, A. Hospital, J. Walther, R. I. Pujagut, F. Battistini, J. L. Gelpi, R. Lavery, and M. Orozco. 2016. Long-timescale dynamics of the Drew-Dickerson dodecamer. Nucleic acids research 44:4052-4066.